

Primordial magnetic fields and the HI signal from the epoch of reionization

Shiv K. Sethi

Raman Research Institute, Sadashivanagar, Bangalore 560080, India

Kandaswamy Subramanian

Inter-University Center for Astronomy & Astrophysics, Post Bag 4, Ganeshkhind, Pune 411007, India

ABSTRACT: The implication of primordial magnetic-field-induced structure formation for the HI signal from the epoch of reionization is studied. Using semi-analytic models, we compute both the density and ionization inhomogeneities in this scenario. We show that: (a) The global HI signal can only be seen in emission, unlike in the standard Λ CDM models, (b) the density perturbations induced by primordial fields, leave distinctive signatures of the magnetic field Jeans' length on the HI two-point correlation function, (c) the length scale of ionization inhomogeneities is $\lesssim 1$ Mpc. We find that the peak expected signal (two-point correlation function) is $\simeq 10^{-4} K^2$ in the range of scales 0.5–3 Mpc for magnetic field strength in the range 5×10^{-10} – 3×10^{-9} G. We also discuss the detectability of the HI signal. The angular resolution of the on-going and planned radio interferometers allows one to probe only the largest magnetic field strengths that we consider. They have the sensitivity to detect the magnetic field-induced features. We show that the future SKA has both the angular resolution and the sensitivity to detect the magnetic field-induced signal in the entire range of magnetic field values we consider, in an integration time of one week.

Contents

1. Introduction	1
2. Magnetic fields in the post-recombination era	2
3. Reionization	3
4. The global HI signal	4
5. Fluctuating component of HI signal	6
5.1 Density and ionization correlation functions	6
5.2 Effect of Large-scale density field on ionization inhomogeneities	8
6. Results: Fluctuating component	9
6.1 Detectability of the signal	10
7. Summary and Conclusions	11

1. Introduction

Understanding the epoch of reionization is one of the outstanding challenges of modern cosmology. In recent years, a partial understanding of this important stage in the history of the universe has emerged. Gunn-Peterson tests have revealed the existence of neutral hydrogen (HI) at redshifts $z \gtrsim 5.7$ ([1, 2, 3, 4, 5]). The detection of temperature-polarization cross-correlation and the polarization-polarization correlation at large angular scales ($\ell \lesssim 10$) in the WMAP data have given firm evidence that the universe reionized around $z \simeq 10$ (e.g. [6]).

The most direct approach to studying this epoch is to attempt to detect the redshifted 21-cm line of the neutral hydrogen during the period when the universe makes a transition from being fully neutral to fully ionized. There is substantial on-going effort in that direction and this also remains one of the primary goals of upcoming and future radio interferometers (e.g. MWA, for a detail description see [7], LOFAR ¹, and SKA ²). Primordial tangled magnetic fields can substantially alter the scenario of structure formation of the universe ([8], hereafter Paper I and references therein). It has been shown that magnetic field-induced structure formation can cause early reionization (Paper I, [9]) and might leave detectable signatures in the HI signal from the epoch of reionization ([10, 11]).

In this paper, we study the implications of the existence of the primordial magnetic fields for possible studies of the reionization epoch. We compute both the global HI signal and its fluctuating

¹www.lofar.org

²www.skatelescope.org/pages/page_sciencegen.htm

component. In particular, we study in detail the nature of ionization inhomogeneities in the presence of magnetic fields, as their precise understanding is needed to correctly set the scale of the effect. The detailed quantification of this aspect constitutes the main difference between our present work and earlier studies. We also discuss in detail the detectability of the magnetic field-induced HI signal.

In §2, we briefly review the salient features of the structure formation process in the presence of primordial tangled magnetic fields. In §3, we give results for the reionization process. In §4, we compute and discuss the global HI signal. In §5 and 6, the fluctuating component of the HI signal is derived and discussed. The detectability of the resultant signal is also discussed. Section 7 is reserved for summary and conclusions. In this paper we use the parameters of the FRW model as favoured by the recent WMAP results [6]: spatially flat FRW model with $\Omega_m = 0.3$ and $\Omega_\Lambda = 0.7$ with $\Omega_b h^2 = 0.022$ and $h = 0.7$ [12].

2. Magnetic fields in the post-recombination era

Sethi and Subramanian (2005) [8] analysed two possible effects of the presence of primordial magnetic fields in the post-recombination era: (a) magnetic fields can induce formation of early structures, (b) the dissipation of magnetic field energy owing to ambipolar diffusion and decaying turbulence can significantly alter the thermal and ionization history.

The main difference between the standard Λ CDM models and the magnetic field-aided structure formation is that, in the latter case, the magnetic field induces additional matter density fluctuations whose power spectrum is given by: $P(k) \propto k^n$ for $k \leq k_J$. Here $k_J \simeq 15(10^{-9} \text{ G}/B_0) \text{ Mpc}^{-1}$ is the magnetic field Jeans' wave number. The matter power spectrum spectral index n tends to one as the magnetic field spectral index approaches -3 (for details and discussion see e.g. [13, 8]). Throughout this paper we use magnetic field power spectrum index -2.9 , which gives $n \simeq 1.1$.

This results in more power at smaller scales as compared to the standard Λ CDM case. In Paper I [8], we showed that the 1σ collapse of structures is possible at large redshifts; the collapse redshift of dark matter haloes is sensitive to the spectral index of the magnetic field power spectrum even though it is fairly independent of the magnetic field strength. It was also shown that the mass dispersion $\sigma(R) \propto 1/R^2$ for scales above the Jeans' mass scales, which is a much sharper fall than the usual case. This means that most of the power is concentrated around scales close to magnetic Jeans' scales. These considerations also give strong indication that the only allowed tangled primordial field models are the ones for which $n \simeq -3$ ([8, 13]).

The magnetic field dissipation in the post-recombination era can also significantly alter the thermal Jeans' length scale, by heating the matter up to $T_m \simeq 10^4 \text{ K}$, depending on the value of the magnetic field strength. Therefore, in this scenario, there is a play-off between early structure formation owing to enhanced power at small scales and suppression of power owing to magnetic field Jeans' scales and the enhanced thermal Jeans' scale (for details see [14]). Taking into account all of these effects, the interesting range of magnetic field strength is: $3 \times 10^{-10} \text{ G} \leq B_0 \leq 3 \times 10^{-9} \text{ G}$. We study here the effects of primordial magnetic fields which are in the above range.

3. Reionization

We model the reionization of the universe as described in Sethi (2005) [15](for more details see [16]). In this model, an HII sphere is carved around collapsed haloes. Reionization proceeds as more sources are born and as the radius of the HII region around each source increases. It is completed when the HII regions coalesce. In this scenario, the ionized fraction at any redshift is given by:

$$f_{\text{ion}}(z) = \frac{4\pi}{3} \int_0^z dz' \int dM \frac{d^2n}{dM dz'}(M, z') R^3(M, z, z') \quad (3.1)$$

This expression remains valid until $f_{\text{ion}} \simeq 1$. Here the mass function dn/dM is computed using the Press-Schechter formalism. The radius of the HII region R is computed by following its evolution around a source with a given photon luminosity \dot{N}_γ (in sec^{-1}) which is assumed to grow linearly with the halo mass; we fix the fiducial value of the photon luminosity to be $\dot{N}_\gamma(0)$ at the mass scale $M = 5 \times 10^7 M_\odot$ (see e.g. [15]). The radius of the evolving HII region is given by (e.g. [17, 15]):

$$\frac{dR}{dt} - HR = \frac{(\dot{N}_\gamma - (4\pi/3)R^3\alpha_B C n_b^2 x_{\text{HI}})}{(\dot{N}_\gamma + 4\pi R^2 x_{\text{HI}} n_b)} \quad (3.2)$$

Here α_B is the case B recombination coefficient, n_b is the background density of baryons (excluding the helium atoms), and C is the clumping factor. We further assume the photon luminosity to be exponentially suppressed with time constant of one-tenth of the Hubble time at the redshift at which the source is born. The other parameter used in the evolution of the HII region around each source is the average clumping factor C ; we assume $C = 2$ in the entire redshift range.

As noted above, the mass function of objects in the magnetic field-aided collapse of structures is expected to have much larger number of objects close to the magnetic Jeans' scale as compared to the usual case, with this number falling sharply at larger scales. Tashiro & Sugiyama (2006a) [9] computed the reionization history in this case and showed that reionization is possible with star-formation efficiency markedly lower than in the usual case. We re-look at this issue within the framework of the semi-analytic approach described above, which explicitly takes into account the growth of HII bubbles around sources.

We show our results in Figure 1. In the Figure, we plot reionization history for two values of magnetic field strength and the usual case with zero magnetic fields. We adopt $\dot{N}_\gamma(0) = \{4 \times 10^{48}, 10^{49}\} \text{sec}^{-1}$ for the two magnetic field cases shown in the figure, respectively with $B_0 = 3 \times 10^{-9} \text{G}$ and $B_0 = 10^{-9} \text{G}$. For the standard case with zero magnetic field we take $\dot{N}_\gamma(0) = 2.5 \times 10^{50}$. All the reionization histories are normalized to the WMAP result $\tau_{\text{reion}} = 0.1$.³

Photon luminosity can be cast in terms of the star formation efficiency, f_{eff} and escape fraction of hydrogen-ionizing photons f_{esc} from star-forming haloes (for more details see [18], p57). A photon luminosity of $\dot{N}_\gamma(0) = 2 \times 10^{50}$ corresponds roughly to $f_{\text{esc}} f_{\text{eff}} = 0.01$ if the photons are emitted over a period one tenth of the Hubble time at $z \simeq 10$, using Scalo IMF. This means that reionization in the standard zero field case requires both the star formation efficiency and escape fraction of roughly 10%. The product of these two parameters could be nearly two orders of

³We note that τ_{reion} is the integrated value between $30 \geq z \geq 0$, to be relevant for the WMAP results. Owing to magnetic field dissipation, partial reionization can lead to a much larger 'reionization' optical depth at much higher redshifts. However, WMAP results are not sensitive to such early partial ionization (Paper I)

magnitude smaller if $B_0 \simeq 3 \times 10^{-9}$ G. Thus one needs a much lower efficiency of star formation for models with primordial magnetic fields. As both these parameters are highly uncertain our analysis doesn't allow us to constrain the magnetic field models from WMAP results alone (e.g. [18]). However, we note here that future meaningful constraints on the star formation efficiency and escape fraction could be used to rule/bear out magnetic field-induced reionization.

We discuss briefly each of the case of magnetic field-induced reionization:

$B_0 \lesssim 5 \times 10^{-10}$ G: In this case, the objects that cause reionization are in the mass range \leq a few $10^7 M_\odot$ or these are molecular-cooled haloes (for a review see e.g. [18]). There are many aspects to the nature of reionization caused by these objects that deserve further attention: (a) the temperature of the regions of the universe that are already (photo)ionized is $\simeq 10^4$ K; this results in a thermal Jeans' mass too high to allow for baryonic collapse and star formation in molecular-cooled haloes in these regions. This means that as the reionization proceeds, in an increasingly larger fraction of the universe, baryonic collapse and star formation is suppressed for haloes with masses $\lesssim 10^8 M_\odot$. Thus there is a quenching in the formation of new star forming haloes as the reionization proceeds. We take into account this process in computing the reionization history. (b) It has been argued that the UV light from the first objects can destroy the molecular hydrogen in the neighbouring haloes, thereby shutting off the process of further collapse and star formation in these haloes [19]. In Sethi, Nath, and Subramanian (2008) [14], we showed that in the presence of primordial magnetic fields, the changed ionized history results in a sharp increase in the formation of molecular hydrogen both in the IGM and in the collapsing halo. For magnetic field strength $B_0 \geq 5 \times 10^{-10}$ G, the molecular hydrogen in the IGM might be sufficient to block the UV light from penetrating the IGM ([20, 14]). (c) Owing to the dissipation of the magnetic field energy in the post recombination era, the change in the thermal history of the universe can increase the thermal Jeans' mass. We take into account this change in our analysis.

$B_0 \geq 10^{-9}$ G: In these cases, the collapsing haloes are in the mass range which allow both molecular and atomic cooling. This means that the impact of quenching, destruction of molecular hydrogen, and the increase in thermal Jeans' length discussed above is less pronounced [14].

4. The global HI signal

The global HI signal is observable at the redshifted HI hyperfine transition. The signal can be seen against the CMBR, the only radio source at high redshifts. The observable deviation from the CMBR temperature at any frequency $\nu_0 = 1420/(1+z)$ MHz is (e.g. [21, 22, 15]):

$$\Delta T_{\text{CMBR}} = -\frac{\tau_{\text{HI}}}{(1+z)}(T_{\text{CMBR}} - T_s) \quad (4.1)$$

The spin temperature T_s is given by [23]:

$$T_s = \frac{T_{\text{CMBR}} + y_c T_K + y_\alpha T_\alpha}{1 + y_c + y_\alpha} \quad (4.2)$$

Here T_K is the matter temperature and T_α is the colour temperature of the radiation close to the Lyman- α line. In the context of the problem at hand, $T_\alpha = T_K$ [24, 25]. y_α determines the contribution of Lyman- α radiation in the determination of the spin temperature; $y_\alpha \simeq 0$ before the

onset of the epoch of reionization. τ_{HI} is given by (e.g. [22, 15] and reference therein):

$$\tau_{\text{HI}} = 0.02 \left(\frac{\Omega_{\text{HI}} h^2}{0.024} \right) \left(\frac{0.15}{\Omega_m h^2} \right)^{1/2} \left(\frac{T_{\text{CMBR}}}{T_s} \right) \left(\frac{1+z}{20} \right)^{1/2} \quad (4.3)$$

Here $\Omega_{\text{HI}} = \rho_{\text{HI}}/\rho_c$ is the density parameter corresponding to the neutral fraction of hydrogen.

The main difference between the standard zero field case and the magnetic field model is in the thermal history of the universe. The dissipation of tangled magnetic fields can significantly alter the thermal history of the universe (Paper I). The other difference is that the build-up of the Lyman- α radiation during the reionization era depends on the mass function of collapsed haloes, which in our case is computed using the magnetic field-induced matter power spectrum. 'Lyman- α ' here refers to the continuum radiation between Lyman- α and Lyman- β frequencies. The photons in this frequency range escape into the medium without getting absorbed by either the emitting source or the HI in the IGM until these photons redshift to a frequency very close to the Lyman- α resonant line frequency (for details e.g. [15] and references therein). We model this effect, as in Sethi (2005) [15], by following the evolution mean specific intensity of the Lyman- α radiation:

$$I_{\nu_\alpha}(z) \simeq \frac{H_0^{-1} h c (1+z)^3}{4\pi \Omega_m^{1/2}} \int dM \int_z^{z_{\text{max}}} dz' \frac{d^2 n}{dM dz'} \dot{N}_{\gamma\alpha}(M, z') (1+z')^{-5/2-\beta} \quad (4.4)$$

Here $\dot{N}_{\gamma\alpha}$ is the Lyman- α photon luminosity of an object and β is the spectral index of the photons in the frequency range between Lyman- α and the Lyman- β . Here $1+z_{\text{max}} = (1+z)\nu_\beta/\nu_\alpha$ and is determined from the knowledge that photons with an energy above the Lyman- β are absorbed locally (see e.g. [26, 27]). Given the uncertainty about the spectrum of the ionizing sources, we assume $\beta = 0$ and $\dot{N}_{\gamma\alpha} = A\dot{N}_\gamma$ i.e. the 'Lyman- α ' photon luminosity is a constant multiple of the luminosity of the Hydrogen-ionizing photons (for more details see the discussion following Eq. (10) in Sethi 2005 [15]).

We show in Figure 2 the global HI signal in the post-recombination era for $A = 20$, the ratio of Lyman- α to hydrogen-ionizing luminosity. The HI signal for one model with zero magnetic field is also shown; the zero magnetic field case shown corresponds to $A = 20$ with spectral index at energies exceeding Lyman-limit $\alpha = 2$ (for further details see [15]), and is normalized to the three year WMAP results. The figure shows that unlike the usual case with zero magnetic fields, the HI signal in the magnetised universe is only observable in emission throughout the post-recombination era. This is mainly because the matter temperature doesn't falls below the CMBR temperature for the magnetic field models we consider (see also [11]).

Different features of Figure 2 can be understood in terms of the altered thermal history in the presence of the magnetic field. The dissipation of the magnetic in the post-recombination era (for details see [8]) raises the matter temperature above the CMBR temperature. As the spin temperature (Eq. 4.2) is determined by matter temperature at high redshifts, the HI signal is observable in emission at high redshifts. This should be contrasted with the standard case in which the HI is observable only in absorption during the pre-reionization era (Figure 2).

As the redshifts decreases, the dilution of the gas density drives the spin temperature towards CMBR temperature. The HI signal therefore approaches zero before the onset of the epoch of reionization. As the reionization epoch sets in, the spin temperature gets coupled to the Lyman- α

radiation, which results in the spin temperature being driven towards matter temperature again. In the standard case, depending on the details of the onset of reionization, the HI could be observable in absorption just as the reionization begins, as is seen in Figure 2 (see e.g. [15, 28]). However, in the magnetic field case, the signal is only observable in emission, as the matter temperature remains above the CMBR temperature. This part of the signal is potentially more promising, as it occurs at frequencies more accessible to the on-going and future experiments. The lack of detection of the HI in absorption therefore could signal the presence of magnetic fields.

In both the standard as well the magnetic field case, the HI signal is observable in emission during most of the phase of reionization, with the signal strength almost independent of spin temperature as the limit $T_s \gg T_{\text{CMBR}}$ is reached.

5. Fluctuating component of HI signal

Here we analyse this signal in terms of two-point correlation function of the HI signal in real space. The correlation function can be expressed as (see e.g. [29]):

$$\begin{aligned} C(r_{12}, \theta) &\equiv \langle \Delta T(\hat{n}_1, r_1) \Delta T(\hat{n}_2, r_2) \rangle = \\ &= T_0(r_1) T_0(r_2) [\langle \psi(\hat{n}_1, r_1) \psi(\hat{n}_2, r_2) \rangle - \langle \psi \rangle^2], \end{aligned} \quad (5.1)$$

with

$$\psi = x_{\text{H}}(\mathbf{r}) [1 + \delta(\mathbf{r})]. \quad (5.2)$$

Here $r_{12} = |\mathbf{r}_1 - \mathbf{r}_2|$ and θ is the angle between the line of sight \hat{n} and the vector $\mathbf{r}_1 - \mathbf{r}_2$ separating the two points, and brackets denote average over \mathbf{r}_1 (the correlation function could be written equivalently as a function of the separation angle between the two points and the frequency difference $\nu_2 - \nu_1$).

The expression in the square brackets in Eq. (5.1) can be further simplified to (for details see [29, 30]):

$$\langle \psi \psi \rangle - \langle \psi \rangle^2 = \xi_{xx} \xi_{\delta\delta}(r_{12}, \theta, z) + \xi_{xx} - \bar{x}_{\text{H}}^2 \quad (5.3)$$

Here $\xi_{\delta\delta} = \langle \delta(\mathbf{r}_1) \delta(\mathbf{r}_2) \rangle$ is the two-point correlation function of the total density contrast, and $\xi_{xx} = \langle x_{\text{H}}(\mathbf{r}_1) x_{\text{H}}(\mathbf{r}_2) \rangle$ is the correlation function owing to the inhomogeneities of the neutral fraction. For further detail on the assumptions made in deriving Eqs. (5.1)-(5.3) and the meaning of relevant variables see e.g. [30].

5.1 Density and ionization correlation functions

The density correlation function, in the linear regime, can be expressed as (e.g. [32, 31, 30]):

$$\begin{aligned} \xi_{\delta\delta}(r_{12}, \theta, z) &\simeq \xi_{\delta\delta}(r_{12}, 0, z) \left(1 + \frac{2}{3}\beta + \frac{1}{5}\beta^2 \right) + \\ &+ \xi_{\delta\delta}(r_{12}, 2, z) \left(\frac{4}{3}\beta + \frac{4}{7}\beta^2 \right) P_2(\theta) \end{aligned} \quad (5.4)$$

Here $\beta \simeq \Omega_m^{0.6}/b$, b is the bias of HI distribution with respect to the matter distribution dominated by the cold dark matter. $P_2(\theta)$ is the Legendre function with $\ell = 2$, and

$$\xi_{\delta\delta}(r, 0, z) = \frac{D_+^2(z)}{2\pi^2} \int dk k^2 P_{HI}(k) j_0(kr) \quad (5.5)$$

$$\xi_{\delta\delta}(r, 2, z) = -\frac{D_+^2(z)}{2\pi^2} \int dk k^2 P_{HI}(k) j_2(kr). \quad (5.6)$$

Here $D_+(z)$ is the growing mode of density perturbations and $P_{HI}(k)$ is the HI power spectrum; we compute it as: $P_{HI}(k) = b^2 P(k)$, where $P(k)$ is the underlying matter power spectrum. Throughout we use $b = 1$.

As discussed above, we envisage the growth of reionization as expansion and coalescence of spherical ionized bubbles around each source. In this scenario, the two-point correlation function of the HI distribution is non-zero even in the absence of density perturbations. The scale of ionized inhomogeneities is determined by the scale of the ionized bubbles.

If we assume all these spherical bubbles to be randomly distributed and non-overlapping (we will discuss this assumption below), then for bubble of size R , one can derive [31, 30]:

$$\xi_{xx} = \frac{\bar{x}_H^2}{(1 - p_{\text{same}}(R))}, \quad (5.7)$$

with

$$p_{\text{same}} = (1 - \bar{x}_H) f(r, R). \quad (5.8)$$

and

$$f(r, R) = 1 - \frac{3r}{4R^3} \left(R^2 - \frac{1}{12} r^2 \right), \quad (5.9)$$

for $r \leq 2R$ and zero otherwise. Here p_{same} is the probability that both points in the computation of the two point correlation function lie in the same ionized bubble. This formalism can be readily extended to bubbles of difference sizes if the bubbles are non-overlapping by adding contributions from bubbles of different sizes (see e.g. [30]):

$$p_{\text{same}}(r) = \sum_R g(R) f(r, R) \quad (5.10)$$

Here $g(R)$ is the distribution function of the radii of the HII regions, normalized such that its integral over all bubble sizes is the average ionized fraction: $\int g(R) = f_{\text{ion}}$.

We show in Figure 3 the distribution function of bubble sizes $g(R)$ at epochs when the average ionized fraction is $f_{\text{ion}} = 0.5$ (left panel) and $f_{\text{ion}} = 0.15$ (right panel) (at redshifts $z \simeq \{10, 12.5\}$, respectively; see Figure 1), for models with magnetic field values of $B_0 = 5 \times 10^{-10}$ G (solid curves) and $B_0 = 3 \times 10^{-9}$ G (dashed curves). The dashed-dotted curves correspond to the zero magnetic field case.

From Figure 3, we notice the following main differences between the magnetised and nonmagnetised models: (a) the sizes of bubbles are much smaller in the case of the magnetic field-induced reionization and (b) the distribution of bubbles radii is far broader in the standard zero magnetic field case. Both these differences are due to the difference in the matter power spectrum in the two cases. As already noted above, most of the haloes are formed close to the magnetic Jeans'

length in the magnetic field case. In the usual case, the power is distributed over a wider range of scales. Also, as pointed out above, the scale of HII regions is smaller in the magnetic field case because most haloes are close to $1\text{-}\sigma$ events and therefore the number of collapsed haloes is larger and the \dot{N}_γ is smaller, as compared to the usual case. An important result of this paper is that the size distribution of HII regions is almost independent of the magnetic field strength as also seen in Figure 3. Even though the mass of the collapsed haloes are larger with increasing magnetic field strength, their luminosities have to be appropriately lowered to normalize to WMAP results, as already noted in a previous section. The results shown in Figure 3 for the magnetic field models are therefore generic and we note here that we did not find any exception to these features in a wide variety of models we studied.

5.2 Effect of Large-scale density field on ionization inhomogeneities

The results of Figure 3 implicitly assume that the positions of ionizing sources are uncorrelated. This however is generally a poor assumption. In the usual case, it has been shown that the scale of bubbles is generally much larger than the assumptions of Figure 3, and the scale of ionization bubble also evolves very rapidly (e.g. [33, 34]). This is also known to be in agreement with simulations (e.g. [37, 35, 36]). In the usual ΛCDM case, the local density power spectral index in the range of scales of interest to the reionization generally lies in the range -3 to -1 , or the density field is strongly correlated for a large range of scales. This means that the impact of the large scale density field on the HII region size is pronounced. Also, the first objects to form are rare objects ($\simeq 2.5\sigma$), which means the centers of ionizing sources are more strongly correlated than the underlying density field.

In the magnetic field case, the density power spectral index is $\simeq 1$ above the magnetic Jeans' mass scale, or the density perturbations are strongly suppressed on scales larger than this scale. Also the first objects to collapse are close to 1σ events which means the centers of the ionizing sources are less correlated. This means that the effect of the large scale density field in this case is likely to be less pronounced. However, we still need to take it into account to assess its impact. We follow here the prescription of Furlanetto, Zaldarriaga, and Hernquist (2004) [34].

Furlanetto et al. (2004) [34] showed that the comoving number density of the HII regions with masses in the range M and $M + dM$ can be expressed as:

$$M \frac{dn}{dM} = \sqrt{\frac{2}{\pi}} \frac{\rho_b}{M} \left| \frac{d \ln \sigma}{d \ln M} \right| \frac{B_0}{\sigma} \exp(-B^2(M, z)/(2\sigma^2)). \quad (5.11)$$

Here $B(M, z) = B_0 + B_1 \sigma^2$ with $B_0 = \delta_c(z) - \sqrt{2}K(\zeta)\sigma_{\min}$ and $B_1 = K(\zeta)/(\sqrt{2}\sigma_{\min})$; $K(\zeta) = \text{erf}^{-1}(1 - \zeta^{-1})$ and σ_{\min} corresponds to the mass dispersion at the size of the smallest halo that can cause reionization. We assume this mass to be $M \simeq 5 \times 10^7 M_\odot$ throughout. The parameter ζ is the ratio between the ionized fraction and the collapsed fraction at any given redshift. As ζ tends to one, the mass function of the HII regions approaches the standard Press-Schechter mass function. This is the limit in which the HII regions enclose a single ionizing sources, and therefore is expected to approximate the results shown in Figure 3. However, ζ is generally much greater than one, which means the HII regions enclose multiple ionizing sources, and their sizes evolve far more rapidly than the prescription of Figure 3.

The size distribution of HII bubbles is given by the single parameter ζ in this formulation. This parameter would generally depend on various physical parameters e.g. photon luminosity of collapsed haloes, clumping factor, etc, and in general will evolve depending on the history of reionization. In other words, the computation of HII regions sizes would require a physical model of the evolution of the ionized fraction. In this paper, we compute this parameter as the ratio of ionized fraction to the collapsed fraction at any redshift from the the semi-analytic model described in section 2, for the ionization history shown in Figure 1.

In Figure 4, we show the distribution of HII region sizes for two values of fractional ionization, f_{ion} and three values of magnetic field strength. The values of ζ , in increasing order of the strength of the magnetic field, are: $\simeq \{10, 14\}, \{9, 12\}, \{4, 7\}$, with each pair of values corresponding to the ionized fraction $f_{\text{ion}} \simeq \{0.15, 0.5\}$. These results should be compared to Figure 3. We notice that HII regions sizes are larger and evolve more strongly. However, as compared to the usual case (e.g. Figure 4 of [34]), the evolution is not as strong for the reasons discussed earlier in the section.

We use the results of Figure 4 to compute the fluctuating component of the HI signal owing to ionization inhomogeneities.

6. Results: Fluctuating component

We show the two-point correlation function of the HI fluctuation in Figure 5 for several magnetic field models. All the curves are for $\theta = \pi/2$ (Eq. (5.4)), that is they basically focus on the angular correlation function. We also break the contribution owing to the density and ionization inhomogeneities (the former corresponds to the first term in Eq. (5.3) and the latter to the next two terms in the equation).

The first three panels of Figure 5 (counterclockwise from bottom) correspond to signals which arise for magnetic field values: $\{B_0 = 5 \times 10^{-10}, 10^{-9}, 3 \times 10^{-9}\}$ G, respectively. The dashed curves give the contribution of the first term in Eq. (5.3), that is $\xi_{xx}\xi_{\delta\delta}^B$, where $\xi_{\delta\delta}^B$ is the correlation function of the purely magnetically induced density perturbations. The dot-dashed curves show the contribution of ionization inhomogeneities to the HI correlation function (the $\xi_{xx} - \bar{x}_H^2$ term). The solid curves in these three panels give the sum of both these contributions.

Note that even in the models with primordial fields, there is another contribution to HI fluctuations (and correlations) due to the inflationary induced density perturbations, say referred to as $\xi_{\delta\delta}^{\text{Inf}}$. It should further be pointed out that if the reionization is caused by primordial magnetic field, the photon luminosity of haloes is too small (see discussion on Figure 1 above) for the haloes formed owing to inflationary density perturbation to cause significant contribution. The number of these haloes is too small to be important in the process of reionization. Therefore, the only impact of the inflationary perturbation in the presence of primordial magnetic fields is to add a contribution owing to density perturbations. In the fourth panel (top left panel of Figure 5), we show the contribution ($\xi_{xx}\xi_{\delta\delta}^{\text{Inf}}$) as a dotted line. The solid line in the fourth panel shows the result of adding this contribution as well to the magnetically induced signals with $B_0 = 3 \times 10^{-9}$ G. Thus it shows the predicted total HI correlation function from all sources of density and ionization fluctuations for the case $B_0 = 3 \times 10^{-9}$ G.

The results shown in Figure 5 can be summarized as follows:

1. The typical scale of ionization inhomogeneities is $\lesssim 1$ Mpc for the magnetic field models. This results follows from the nature of distribution function of HII regions, as shown in Figure 4.
2. Ionization inhomogeneities make a comparable contribution to HI fluctuation signals as that arising from density perturbations. For smaller values of magnetic fields, the ionization inhomogeneities can also provide the dominant contribution of the signal.
3. The HI correlation function arising from density fluctuations show characteristic oscillations, with a scale length which increases with increasing value of the magnetic field strength. This is expected as the dominant contribution to the signal comes from scales close to the magnetic Jeans' length. Detecting such oscillations could give an indication of the influence of primordial magnetic fields and also help in determining the field strength. Also the change in sign of the HI correlation at scales above the scale of ionization inhomogeneities ($r \gtrsim 1$ Mpc) could provide additional information.
4. In Panel 4 of Figure 5 (counter clockwise), we show the total observable signal in the presence of a magnetic field of strength 3×10^{-9} G. As noted above if the magnetic field-induced structure formation is responsible for reionization, ξ_{xx} is totally determined by the primordial field strength, and the only contribution of inflationary generated density perturbations is to add a term of the form $\xi_{xx}\xi_{\delta\delta}^{\text{Inf}}$ to the HI correlations.

The main difference between the usual Λ CDM case and the magnetic field scenario, as also alluded above, is in the scale of the signal. Both the density coherence scale (as seen in the fourth panel of Figure 5) and the scale of ionization inhomogeneities are larger in the Λ CDM case.

The process of reionization can be considerably more complex as compared to the results shown in Figure 1. The ionizing sources can have varying spectral indices, star-formation efficiencies and star formation histories, which could have a non-trivial impact on the photon luminosity in the process of reionization. We have studied a suite of ionization histories in addition to the one shown in Figure 1 and find that the results in Figure 3 and 4 are fairly robust. This behaviour arises due to the fact that the magnetic field scenario is completely dominated by scales around the magnetic Jeans' length. This scale determines both the density inhomogeneities as well as the sizes of HII regions that form.

6.1 Detectability of the signal

As noted above, the main difference between the standard zero field and the magnetic field induced reionization is generally the much shorter correlation length scale of the fluctuating HI signal in the latter case. Many radio interferometers currently being built to observe the epoch of reionization have typical angular resolution of a few arc-minutes ($1' \simeq 2$ Mpc for the cosmological parameters of interest), which corresponds to a linear scale $\simeq 5$ – 10 Mpc.⁴ These experiments are therefore not sensitive to the scales at which magnetic field effects are likely to dominate, except for the largest values of B_0 . MWA is expected to have a primary beam of 20° and synthesized beam of

⁴These experiments have greater resolution in the frequency domain, e.g. MWA can have 4000 channels over 32 MHz band-width, which corresponds to length resolution of $\simeq 15$ kpc

4' with 500 'tiles'. Assuming full UV coverage of the primary beam, the expected error on the estimated two-point correlation function is $\simeq 3 \times 10^{-7} \text{ K}^2$, for an integration time of 10^6 sec (see e.g. [30]). This might allow a detection of the signal, as shown in Figure 5, with magnetic field of strength $B_0 \simeq 3 \times 10^{-9}$. However, we note here that an indirect indication of the presence of magnetic field might be possible. If the reionization was indeed caused by a magnetic field of strength $B_0 \simeq 10^{-9} \text{ G}$, the reionization process would appear to be almost 'homogeneous' at the angular resolution probed by these instruments.

Future radio interferometer SKA has the angular resolution and the frequency coverage to directly detect the redshifted HI fluctuation owing to magnetic fields effects, for the entire range of magnetic field strengths we consider here. SKA is projected to have a point-source sensitivity of $\simeq 400 \mu\text{Jy}$ in one-minute integration (in the continuum mode) in the frequency range of interest (70 MHz and 300 MHz). Assuming a synthesized beam in the range $15''\text{--}30''$, relevant for our study, and a simultaneous sky coverage of 25^0 (the simultaneous sky coverage of SKA is planned to be much larger, which will increase the sensitivity further), the sky brightness sensitivity for the statistical detection (in the line mode) is in the range $10^{-6} \text{ K}^2\text{--}2 \times 10^{-7} \text{ K}^2$ for one month of integration. This suggests that a $5\text{-}\sigma$ detection of the signal shown in Figure 4 should be possible with less than one week of integration with SKA.

7. Summary and Conclusions

Tangled primordial magnetic field can have interesting consequences for cosmology. The presence of these fields leave detectable signatures in the CMBR temperature and polarization anisotropies ([38, 39], [40], [41],[42], [43],[44],[45],[46],[47],[48],[49, 50]). The statistics of this signature will also have distinctive non-Gaussian features [51, 52, 53]. From these considerations, one can obtain an upper limit on the magnetic fields strength $B_0 \lesssim 4 \times 10^{-9} \text{ G}$ [43], for models with magnetic field power spectrum index $n \simeq -3$, which are the only models that are consistent with current state of observations [54, 8].

Sethi & Subramanian (Paper I) considered many aspects of these fields in the post-recombination universe. In particular, they showed that magnetic field-induced structure formation might lead to early reionization and the dissipation of these fields can substantially alter the thermal and ionization history of the universe.

Magnetic field-induced reionization and its possible impact on the detectable HI signal has been considered by several authors [10, 11]. In this paper, we study these aspects further within the framework of semi-analytic models which allow us to compute and add in the impact of reionization inhomogeneities on the HI signal.

Our main findings can be summarized as:

1. Owing to magnetic field dissipation in the post-recombination, the HI signal is not expected to show any absorption features unlike the standard case (Figure 2) (see also [11]).
2. The matter power spectrum owing to magnetic-field induced structure formation is peaked around the magnetic Jeans' scale. This scale is imprinted on the HI signal as typical oscillations in the HI angular correlation function (Figure 5)

3. Figure 5 also captures the impact of ionization inhomogeneities. The scale of the ionization inhomogeneities is $\lesssim 1$ Mpc, for a wide range of magnetic field strengths (Figure 4).
4. We show that the presently-operational and upcoming radio interferometers are sensitive to the magnetic field strength $B_0 \simeq 3 \times 10^{-9}$ G. However, the future SKA will be able to detect the HI signal for the entire range of magnetic field strength: $5 \times 10^{-10} \lesssim B_0 \lesssim 3 \times 10^{-9}$ G. A detection of a characteristic scale and nature of oscillations of the HI correlation function could help measure the magnetic field at these scales directly.

The upcoming SKA will also have the capability of direct detection of primordial tangled magnetic field by measuring the Faraday rotation of $\simeq 10^7$ radio sources.

We note here that the main advantage of a potential detection of the HI signal is that it is sensitive to far smaller values of magnetic field strength as compared to the other probes.

Acknowledgments

We thank an anonymous referee for many useful suggestions.

References

- [1] X. Fan, C. L. Carilli, B. Keating, ARAA, 44, 415, 2006
- [2] R. L. White, R. H. Becker, X. Fan, M. A. Strauss, ApJ, 126, 1, 2003
- [3] S. G. Djorgovski, S. Castro, D. Stern, A. A. Mahabal, ApJL, 560, L5, 2001
- [4] X. Fan, V. K. Narayanan, M. A. Strauss, R. L. White, R. H. Becker, L. Pentericci, H. Rix, AJ, 123, 1247, 2002
- [5] R. H. Becker et al., AJ, 122, 2850, 2001
- [6] D. N. Spergel, et al, ApJS, 170, 377, 2007
- [7] J. D. Bowman, M. F. Morales, J. N. Hewitt, ApJ, 638, 20, 2006
- [8] S. K. Sethi, K. Subramanian, MNRAS, 356, 778, 2005
- [9] H. Tashiro, N. Sugiyama, MNRAS, 368, 965, 2006a
- [10] H. Tashiro, N. Sugiyama, MNRAS, 372, 1060, 2006b
- [11] D. R. G. Schleicher, R. Banerjee, R. S. Klessen, 692, 236, 2009
- [12] W. L. Freedman, et al., ApJ, 553, 47, 2001
- [13] R. Gopal, S. K. Sethi, Journal of Astrophysics and Astronomy, 24, 51, 2003
- [14] S. K. Sethi, B. B. Nath, K. Subramanian, MNRAS, 387, 1589, 2008
- [15] S. K. Sethi, MNRAS, 363, 818, 2005
- [16] Z. Haiman, G. Holder, ApJ, 595, 1, 2003
- [17] J. S. B. Wyithe, A. Loeb, 427, 815, 2004
- [18] R. Barkana, A. Loeb, Phys. Rep., 349, 125, 2001

- [19] Z. Haiman, M. Rees, A. Loeb, *ApJ*, 476, 458, 1997
- [20] Z. Haiman, T. Abel, M. J. Rees, *ApJ*, 534, 11, 2000
- [21] D. Scott, M. J. Rees, *MNRAS*, 247, 510, 1990
- [22] P. Madau, A. Meiksin, M. J. Rees, 475, 429, 1997
- [23] G. Field, *Proc. IRE*, 46, 240, 1958
- [24] G. Field, G., *ApJ*, 129, 551, 1959
- [25] G. B. Rybicki, I. P. Dell’Antonio, *ApJ*, 427, 603, 1994
- [26] Prichard, S. R. Furlanetto, *MNRAS*, 367, 1057, 2006
- [27] C. Hirata, *MNRAS*, 367, 259, 2006
- [28] N. Gnedin, P. Shaver, *ApJ*, 608, 611, 2004
- [29] M. Zaldarriaga, S. R. Furlanetto, L. Hernquist, *ApJ*, 608, 622, 2004
- [30] S. K. Sethi, Z. Haiman, *ApJ*, 673, 1, 2008
- [31] R. Barkana, A. Loeb, *ApJ*, 624, L65, 2005
- [32] S. Bharadwaj, S. S. Ali, *MNRAS*, 352, 142, 2004
- [33] R. Barkana, A. Loeb, *ApJ*, 609, 475, 2004
- [34] S. R. Furlanetto, M. Zaldarriaga, L. Hernquist, *ApJ*, 613, 1, 2004
- [35] I. T. Iliev, G. Mellema, Ue-Li Pen, J. R. Bond, P. R. Shapiro, *MNRAS*, 384, 863, 2008
- [36] M. McQuinn, A. Lidz, O. Zahn, S. Dutta, L. Hernquist, M. Zaldarriaga, *MNRAS*, 377, 1043, 2007
- [37] G. Mellema, I. T. Iliev, Ue-Li Pen, P. R. Shapiro, *MNRAS*, 372, 679, 2006
- [38] K. Subramanian, J. D. Barrow, *PRL*, 81, 3575, 1998
- [39] K. Subramanian, J. D. Barrow, J., *MNRAS*, 335, L57, 2002
- [40] R. Durrer, P. G. Ferreira, T. Kahniashvili, *Phys. Rev. D.*, 61, 043001, 2000
- [41] T. R. Seshadri, K. Subramanian, K., *PRL*, 87, 101301, 2001
- [42] A. Mack, T. Kahniashvili, A. Kosowsky, *Phys. Rev. D* 65, 123004, 2002
- [43] R. Gopal, S. K. Sethi, *Phys. Rev. D*, 72,3003, 2005
- [44] A. Lewis, *Phys. Rev. D*. 70, 43011, 2004
- [45] T. Kahniashvili, B. Ratra, *Phys. Rev. D*, 71, 103006, 2005
- [46] M. Giovannini, *Phys. Rev. D.*, 74, 063002, 2006
- [47] M. Giovannini, K. E. Kunze, *Phys. Rev. D.*, 77, 063003, 2008
- [48] D. G. Yamazaki, K. Ichiki, T. Kajino, G. J. Mathews, *Phys. Rev. D.*, 77, 043005, 2008
- [49] F. Finelli, F. Paci, D. Paoletti, *Phys.Rev.D*, 78,023510, 2008
- [50] D. Paoletti, F. Finelli, F. Paci, *astro-ph:0811.0230*, 2008
- [51] I. Brown, R. Crittenden, *Phys. Rev. D*. 72, 3002, 2005
- [52] T. R. Seshadri, K. Subramanian, *Phys. Rev. Lett.*, 103, 081303, 2009
- [53] C. Caprini, F. Finelli, D. Paoletti, A. Riotto, *JCAP*, 06, 021, 2009
- [54] C. Caprini, R. Durrer, *Phys. Rev. D*, 65, 3517, 2002

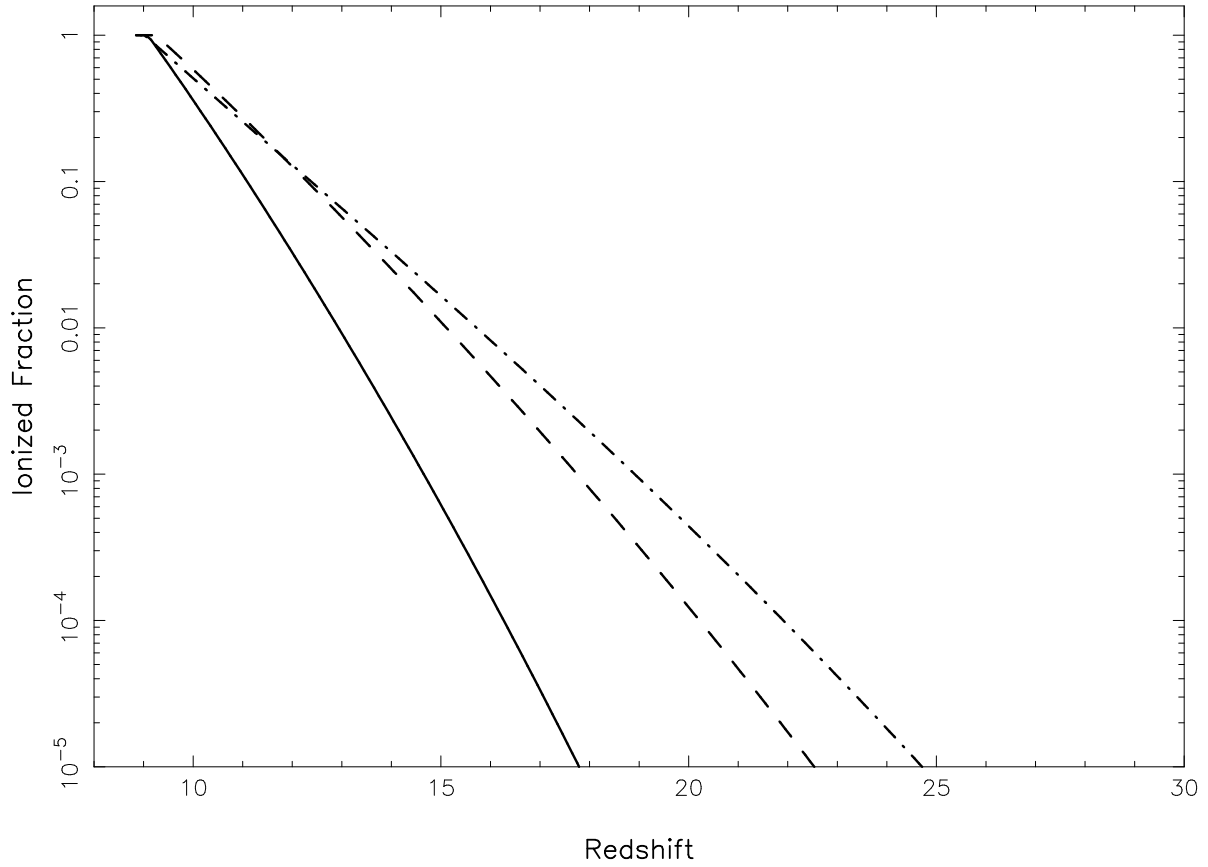


Figure 1: The ionization history of the universe is shown for two magnetic field models along with the usual case without magnetic field. The dashed and the dot-dashed curve correspond to the magnetic field strength $B_0 = \{10^{-9}, 3 \times 10^{-9}\}$ G, respectively. The solid curve correspond to the case without magnetic field. For details about other parameters see the text.

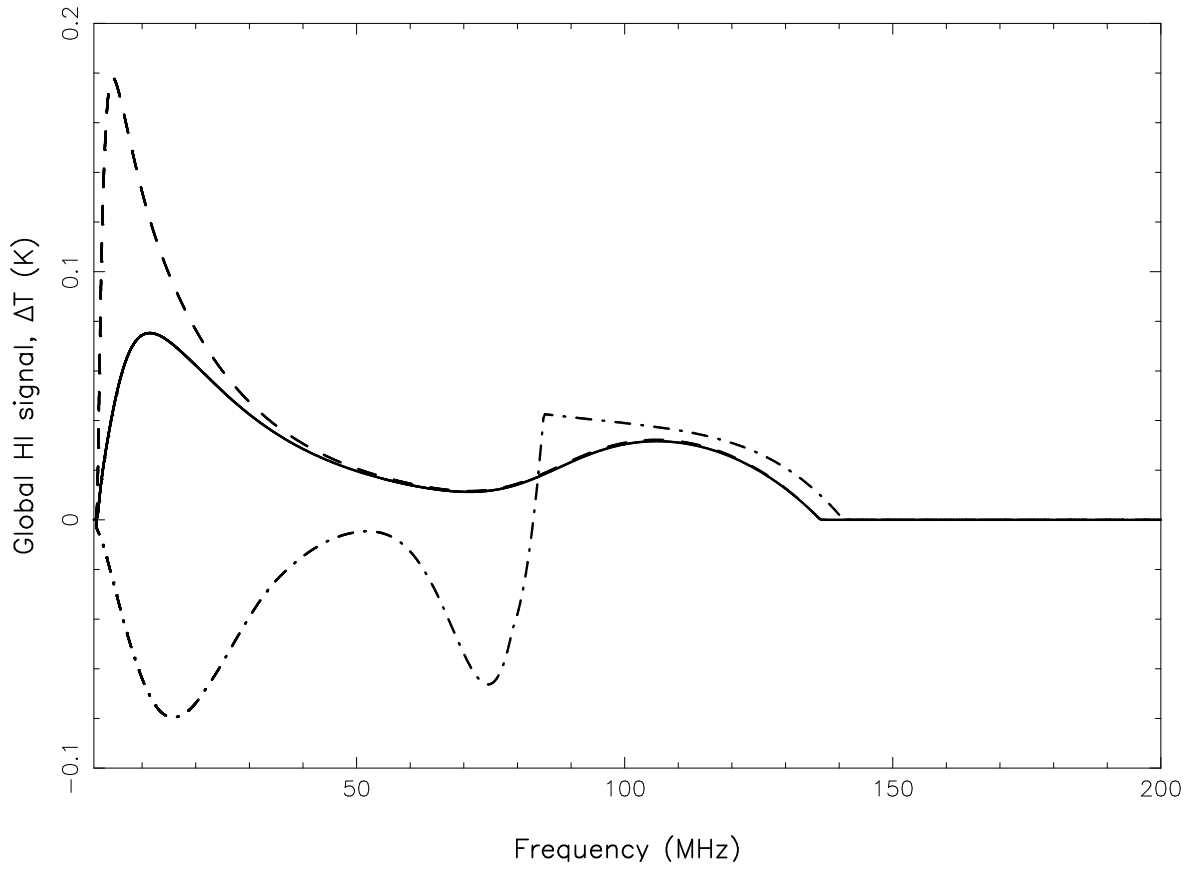


Figure 2: The Global HI signal is shown for two values of magnetic field strengths. The solid and dashed curves correspond to the magnetic field strength $B_0 = \{5 \times 10^{-10}, 10^{-9}\}$ G, respectively. The dot-dashed curve corresponds to HI signal for one possible scenario in the zero magnetic field case (see text for details).

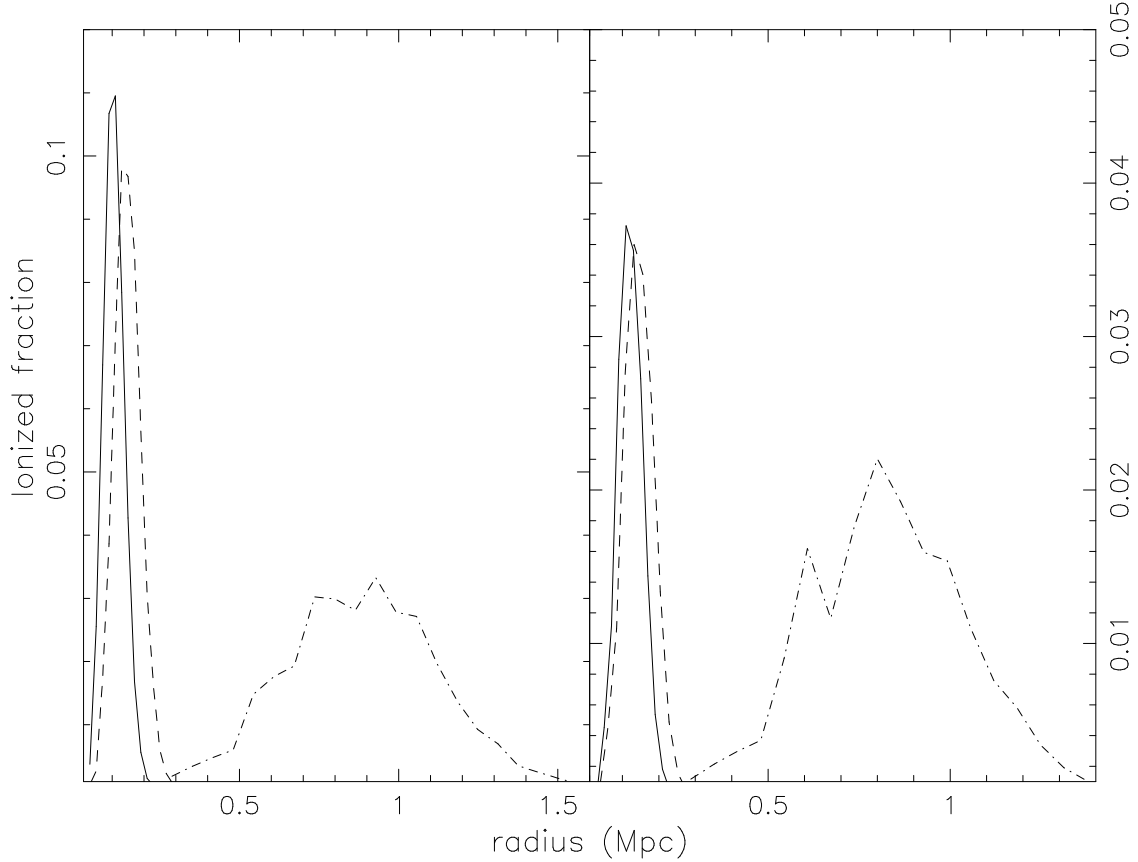


Figure 3: The ionized fraction is shown as function of radius of the HII region. The area under each curves is the ionized fraction. The dot-dashed curve correspond to the case without magnetic field. The solid and dashed curves correspond to the magnetic field strength $B_0 = \{5 \times 10^{-10}, 3 \times 10^{-9}\}$ G, respectively. In the left panel the ionized fraction is $f_{\text{ion}} \simeq 0.5$ and $f_{\text{ion}} \simeq 0.15$ for the right panel, which correspond roughly to the redshifts 10 and 12.5, respectively, as discussed in the text.

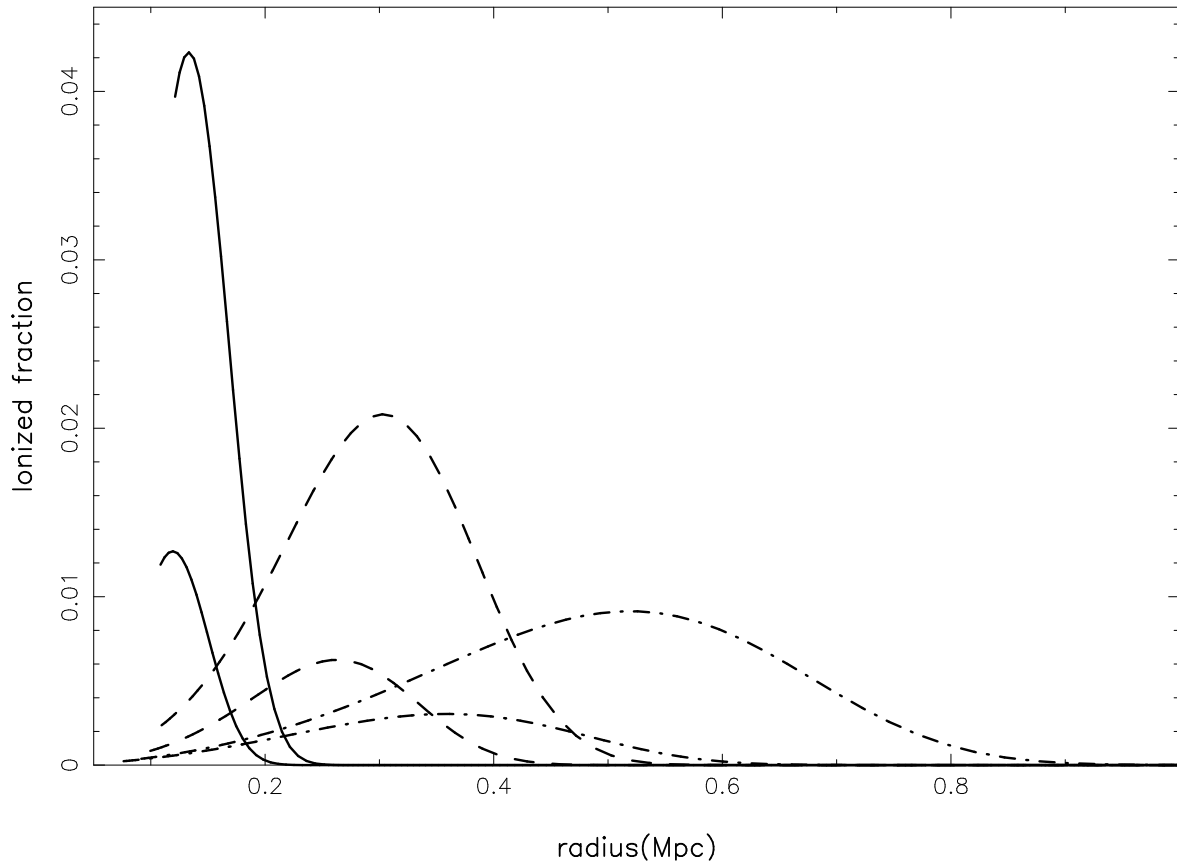


Figure 4: The ionized fraction is shown as function of radius of the HII region. The solid, dashed, and dot-dashed curves correspond to $\{B_0 = 5 \times 10^{-10}, 10^{-9}, 3 \times 10^{-9}\}$ G, respectively. The lower and the upper curve for each line style correspond to $f_{\text{ion}} \simeq 0.15$ and $f_{\text{ion}} \simeq 0.5$, respectively. ζ values for these curves are: $\simeq \{10, 14\}, \{9, 12\}, \{4, 7\}$, with each pair of values corresponding to the two cases of ionized fraction.

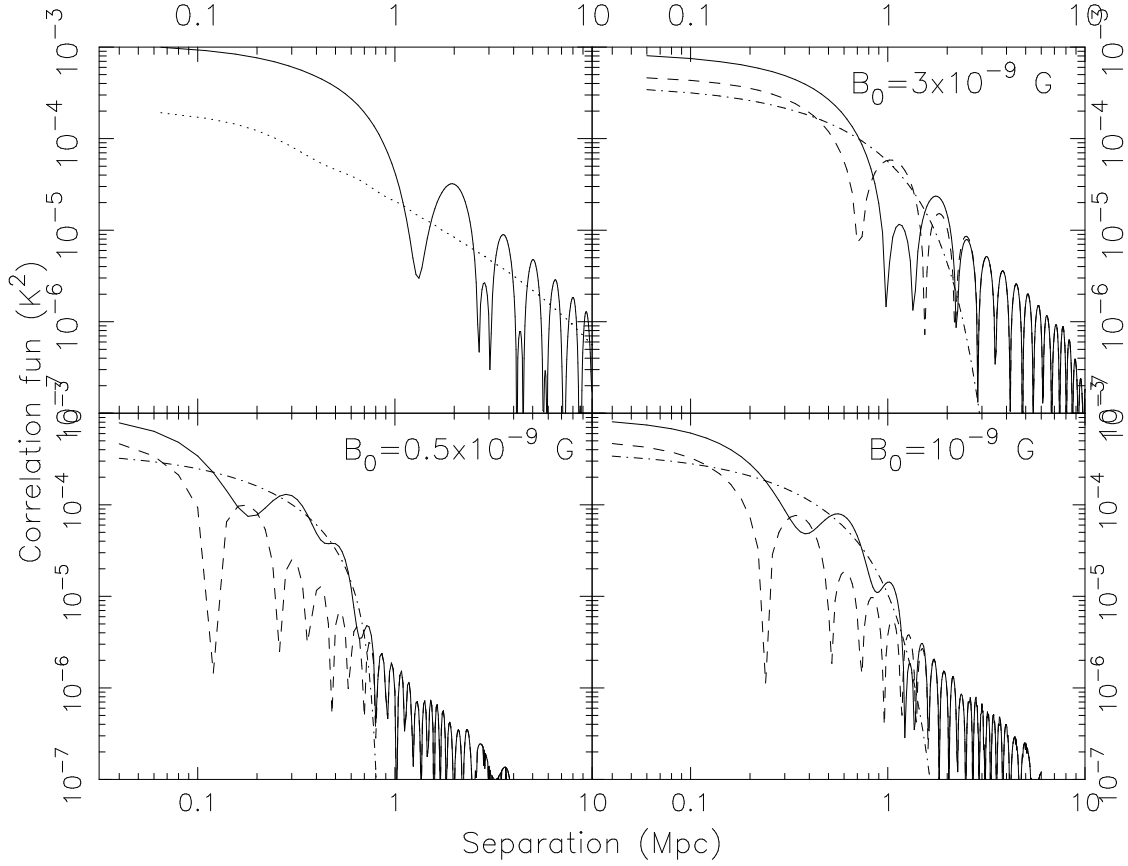


Figure 5: The first three panels (counterclockwise from bottom) correspond to the signal for magnetic field values: $\{B_0 = 5 \times 10^{-10}, 10^{-9}, 3 \times 10^{-9}\}$ G, respectively; The signal corresponds to $f_{\text{ion}} \simeq 0.5$ (Left panel of Figure 3) at $z \simeq 10$. The solid, dashed, and dot-dashed curves correspond to the absolute value of the total signal, the signal owing to density fluctuations, and the signal from ionization inhomogeneities. In the fourth panel, we show the total observable signal (solid line) for $B_0 = 3 \times 10^{-9}$ G, which includes the contribution from density fluctuations in the standard Λ CDM case (dotted line).